Peer reviewed version

Link to published version (if available):
10.1111/gbi.12186

Link to publication record in Explore Bristol Research
PDF-document

University of Bristol - Explore Bristol Research
General rights

A new occurrence of ambient inclusion trails (AITs) from the ~1900 million-year-old Gunflint Formation, Ontario: nano-characterization and testing of potential formation mechanisms

David Wacey,[1,2*] Martin Saunders,[3] Charlie Kong[4] and Matt R. Kilburn[1]

[1]*Australian Research Council Centre of Excellence for Core to Crust Fluid Systems, and Centre for Microscopy Characterisation and Analysis, The University of Western Australia, 35 Stirling Highway, Crawley, WA 6009, Australia.*

[2]*School of Earth Sciences, University of Bristol, Life Sciences Building, 24 Tyndall Avenue, Bristol, BS8 1TQ, UK.*

[3]*Centre for Microscopy Characterisation and Analysis, The University of Western Australia, 35 Stirling Highway, Crawley, WA 6009, Australia.*

[4]*Electron Microscopy Unit, University of New South Wales, Kingsford, NSW 2052, Australia.*

Running title: New AITs from the Gunflint Formation

ABSTRACT

Ambient inclusion trails (AITs) are tubular microstructures thought to form when a microscopic mineral crystal is propelled through a fine-grained rock matrix. Here we report a new occurrence of AITs from a fossilized microbial mat within the 1878 Ma Gunflint Formation, at Current River, Ontario. The AITs are 1–15 μm in diameter, have pyrite as the propelled crystal, are infilled with chlorite, and have been propelled through a micro-quartz (chert) or chlorite matrix. AITs most commonly originate at

the boundary between pyrite- and chlorite-rich laminae and chert-filled fenestrae, with pyrite crystals propelled into the fenestrae. A subset of AITs originate within the fenestrae, rooted either within the chert, or within patches of chlorite.

Sulfur isotope data (^{34}S/^{32}S) obtained *in situ* from AIT pyrite have a δ^{34}S of -8.5 to +8.0 ‰, indicating a maximum of ~30 ‰ fractionation from Palaeoproterozoic seawater sulfate (δ^{34}S ≈ +20 ‰). Organic carbon is common both at the outer margins of the fenestrae and in patches of chlorite where most AITs originate, and can be found in smaller quantities further along some AITs towards the terminal pyrite grain.

We infer that pyrite crystals now found within the AITs formed via the action of heterotrophic sulfate-reducing bacteria during early diagenesis within the microbial mat, as porewaters were becoming depleted in seawater sulfate. Gases derived from this process such as CO_2 and H_2S were partially trapped within the microbial mat, helping produce birds-eye fenestrae, while rapid micro-quartz precipitation closed porosity. We propose that propulsion of the pyrite crystals to form AITs was driven by two complementary mechanisms during burial and low grade metamorphism. Firstly, thermal decomposition of residual organic material providing CO_2, and potentially CH_4, as propulsive gases, plus organic acids to locally dissolve the micro-quartz matrix. Secondly, reactions involving clay minerals that potentially led to enhanced quartz solubility, plus increases in fluid and/or gas pressure during chlorite formation, with chlorite then infilling the AITs. This latter mechanism is novel and represents a possible way to generate AITs in environments lacking organic material.

INTRODUCTION

Ambient inclusion trails (AITs) represent a specific class of microtubular structure that results from the propulsion of small mineral crystals through a rock matrix. They possess a number of defining morphological characteristics that permit their discrimination from superficially similar filamentous microfossils, endolithic microborings, and mineral filaments (Wacey et al., 2008a,b; Mcloughlin et al., 2007, 2010). These features include: the presence of a mineral crystal at the terminal end of the microtube; a polygonal cross section mirroring the crystal geometry of the propelled grain; and striations along the length of the microtube caused by the angular facets of the propelled grain. Further common, but not necessarily diagnostic, morphological features include assemblages of AITs arranged in radial starburst patterns, AITs possessing side-branches of a smaller diameter where the propelled grain has become fragmented, and an increase in curvature toward the terminal end of an AIT (Wacey et al., 2008a).

AITs were first reported over half a century ago from the Palaeoproterozoic Gunflint Formation of North America (Tyler and Barghoorn, 1963), though their history may arguably be traced back decades further when structures resembling AITs were mistakenly thought to be evidence for algal life in the Archean (Gruner, 1923). Despite this half-century or more of study, there remain only a handful of reports of AITs and their formation mechanism is still relatively poorly understood. Here we will provide a brief summary of previous reports of AITs before describing a new

occurrence associated with a microbial mat from the 1878 Ma Gunflint Formation of Ontario. We then use a combination of high spatial resolution *in situ* techniques including transmission electron microscopy (TEM), nano-scale secondary ion mass spectrometry (NanoSIMS) and laser Raman to characterize these new AITs and test possible formation mechanisms.

Previous reports and current understanding of AITs

Although still a rare phenomenon, AITs have been reported from rocks up to 3500 Ma in age, from a range of geological environments, and with a variety of propelled crystals, tubular infillings and host matrices. The oldest AITs come from two chert units of the ~3500-3450 Ma Warrawoona Group of Western Australia (Awramik et al., 1983; Buick, 1990; Wacey et al., 2008b). These are 1-5 μm in diameter, several 10's μm in length, have been propelled through a microcrystalline quartz matrix, and infilled with micro-quartz, iron phosphate or iron oxide. Where terminal crystals are present they are hematite, interpreted as a replacement pseudomorph of pyrite (Awramik et al., 1983).

AITs are also common in slightly younger silicified sediments of the 3430 Ma Strelley Pool Formation and 3240 Ma Kangaroo Caves Formation, Western Australia (Wacey et al., 2008a,b). The former are 1-15 μm in diameter and up to 300 μm in length (Fig. 1a), have pyrite as the propelled grain, occur in a microcrystalline quartz matrix and are infilled with micro-quartz, iron phosphate, aluminum phosphate or jarosite (iron potassium sulfate). The latter are 15-100 μm in diameter and up to 100 μm in length, almost always have a terminal pyrite crystal, occur in a microcrystalline quartz matrix and are infilled with chlorite or micro-quartz (Fig. 1b). The smallest

AITs so far reported come from the ~2700 Ma Fortescue Group, found within a chert at the base of the group (Knoll and Barghoorn, 1974). These are < 1μm in diameter but can be up to 60 μm in length. These are the type example for growth as starburst patterns away from central masses of organic material, occasionally have terminal pyrite crystals, are infilled with iron carbonate, and hosted in a microcrystalline quartz matrix (Fig. 1c).

AITs have also been found in Archean volcanic rocks, including pyroclastic tuff from the 2720 Ma Tumbiana Formation (Lepot et al., 2011) and basalt from the 2700 Ma Maddina Formation (Lepot et al., 2009), both from the Fortescue Group of Western Australia. AITs in the former comprise quartz filled microtubes (up to 20 μm diameter) in volcanic glass and have terminal pyrite crystals. Those in the latter are arranged in a starburst pattern with diameters of 0.5-5 μm and lengths up to 200 μm. They occur in a micro-quartz matrix and are uniquely infilled by andradite garnet with terminal carbonaceous (rather than mineral) grains. Further occurrences in basalt come from the Palaeoproterozoic (~2,000 Ma) Pechenga greenstone belt, Russia (McLoughlin et al., 2013). These AITs comprise small tubes, less than 10 μm in diameter and generally less than 100 μm in length, that radiate into chlorite from a quartz-carbonate interpillow matrix. They possess terminal inclusions of an unknown sulfide mineral. Some AITs in metavolcanic rocks (e.g., types 3 and 4 of Lepot et al., 2011) have been compared to and interpreted as dendrites, crystals grown along preferential axes via diffusion controlled processes during metamorphism (Vernon, 2004).

Also in the Palaeoproterozoic, AITs have been reported from the coeval ~1900 Ma Gunflint Formation, Ontario and the Biwabik Formation, Minnesota (Tyler and Barghoorn, 1963). Here, iron carbonate-filled AITs are up to 10 μm in diameter and 100 μm in length, whereas quartz-filled AITs are particularly large, up to 1.4 mm in diameter and 3 mm in length. In both cases pyrite is the propelled crystal and the matrix is microcrystalline quartz. Chlorite-filled trails of ~30 μm diameter were also observed from iron formations of similar age in Michigan (Tyler and Barghoorn, 1963); here hematite (likely pseudomorphing original pyrite) had been propelled though an iron-rich microcrystalline quartz matrix.

In the Ediacaran period, AITs occur in the ~570 Ma Doushantou Formation of China (Xiao and Knoll, 1999; Xiao et al., 2007; She et al., 2013). Two separate AIT occurrences have been reported: firstly, from phosphatic spheroidal fossils, interpreted to be animal embryos, in the upper Doushantuo Formation at Weng'an (Xiao and Knoll, 1999; Xiao et al., 2007); and secondly, from granular phosphorites in the lower portion of member II of the formation near Yichang (She et al., 2013). In the former, AITs are 10-80 μm in diameter and may be up to 1mm in length, possessing terminal pyrite crystals, longitudinal striations and are not infilled (Fig. 1d). In the latter, rare AITs are around 20 μm in diameter, 100's μm in length, have terminal pyrite or hematite crystals and have been propelled through a calcium phosphate matrix. Moving over the boundary into the Cambrian, large AITs have been reported from the Soltanieh Formation of Iran; these are up to 80 μm in diameter and both the host matrix and infilling is calcium phosphate (Wacey et al., 2008a).

Further AITs have recently been found in the phosphatised valves of crustaceans from the upper Cambrian of Poland and the lower Devonian of The Ukraine (Olempska and Wacey, 2016). These range in diameter from 1-20 μm and can approach 100 μm in length (Fig. 1e). Most of these AITs have terminal pyrite crystals but the microtube behind the crystals is commonly empty so that longitudinal striations are clearly visible along the inner microtube walls. The youngest AITs so far reported come from fish scales within the 390 Ma Achanarras limestone of Northern Scotland (Wacey et al., 2008a). These are 5-12 μm in diameter and up to 150 μm in length and have curved, looped and twisted morphologies. Terminal crystals, where present, are pyrite and organic material is frequently preserved within the microtubes (Fig. 1f). Both the host matrix and microtube infillings are phosphatic. AITs may be much more common than this handful of reported occurrences suggest; for example, reanalysis of several sets of microtubular structures previously interpreted as endolithic borings or 'predatory trace fossils' (e.g., Conway Morris and Bengston, 1994; Stockfors and Peel, 2005; Zhang and Pratt, 2008) suggests that these may be more plausibly interpreted as AITs (Xiao and Knoll, 1999; Olempska and Wacey, 2016). Some problematical Precambrian microfossil-like filaments may also be AITs (Grey, 1986).

This brief summary of AIT occurrences in the geological record shows that they are most common in Precambrian silicified sediments, while in younger rocks phosphate appears to be the preferred host matrix. This may reflect changing ocean chemistry and its effect on the type of mineral phases that form during early diagenesis. Terminal crystals are almost always pyrite (or oxidized products of pyrite) but this may not be ubiquitous (cf. Lepot et al., 2009). The most variable feature of AITs is the mineralogy of the microtube; some remain empty, while quartz, iron carbonate,

calcium/iron/aluminium phosphate, iron-potassium sulfate, garnet, chlorite, and iron oxide may all precipitate behind the moving pyrite crystal. A common association of organic matter and AITs has led to the hypothesis that AITs are formed by degassing of decomposing organic material attached to pyrite (or similar) grains within an impermeable rock matrix during heating associated with late-stage diagenesis and/or metamorphism (Knoll and Barghoorn, 1974; Wacey et al., 2008b; McLoughlin et al., 2010). Questions remain, however, regarding the extent of biological participation in this formation mechanism, the origin of the pyrite crystals and whether other formation mechanisms might also be viable.

This contribution looks at a new occurrence of AITs from the 1878 Ma Gunflint Formation, using high-spatial resolution *in situ* techniques to characterize both the pyrite and microtube at the nano-scale, and to enhance our understanding of AIT formation.

METHODS

Focussed ion beam (FIB) preparation of TEM samples

Prior to FIB preparation, standard polished geological thin sections were examined by optical microscopy, using *Zeiss Axioskop 2 and Nikon Optiophot-pol* microscopes, and scanning electron microscopy (SEM), using a *Zeiss Supra 1555* SEM in order to gain an understanding of AIT distributions and morphologies, and to select the most appropriate targets for detailed study. A dual-beam FIB system (*FEI Nova NanoLab*) at the University of New South Wales was then used to prepare AIT TEM samples from the thin sections coated with ~30 nm of gold. Electron beam imaging within the dual beam FIB was used to identify microstructures of interest in the thin sections

allowing site-specific TEM samples to be prepared. The TEM sections were prepared by a series of steps involving different ion beam energies and currents (see Wacey et al., 2012 for details), resulting in ultrathin wafers of c. 100 nm thickness. These TEM wafers were extracted using an ex-situ micromanipulator and deposited on continuous-carbon copper TEM grids. FIB preparation of TEM sections allows features below the surface of the thin sections to be targeted, thus eliminating the risk of surface contamination producing artefacts.

TEM analysis of FIB-milled wafers

TEM data were obtained using a *FEI Titan G2 80-200* TEM/STEM with *ChemiSTEM Technology* operating at 200 kV, located in the Centre for Microscopy Characterisation and Analysis (CMCA) at the University of Western Australia. Data obtained included bright-field TEM images, HAADF (high angle annular dark-field) STEM images, EDS (*ChemiSTEM*) maps, and selected area electron diffraction patterns (using a 40 μm aperture that selected a 600 nm field of view) for mineral identification.

SEM-EDS

Elemental analysis and mapping over several millimeters of a Current River thin section was performed on a *FEI Verios 460* SEM equipped with an *Oxford Instruments X-Max 80* energy dispersive X-ray spectroscopy (EDS) system and *Oxford Instruments AZtec 3.0* nano-analysis software, located at CMCA.

NanoSIMS sulfur isotope analysis

Sulfur isotope ratios ($^{34}S/^{32}S$) from individual pyrite grains were determined using a CAMECA NanoSIMS 50, located at CMCA. The analyses were performed using a Faraday Cup (FC) detector for the ^{32}S signal and an electron multiplier (EM) for the ^{34}S signal, with a primary beam current of ~3.5 pA, with the NanoSIMS in 'isotope analysis' mode. NanoSIMS parameters were configured to give a workable amount of signal for the ^{34}S isotope (for example, ES=2, AS=0, Ens=10%, D1=2 gave c. 70,000 counts per second for ^{34}S). Charge compensation was not necessary in this case. Isotope data were acquired by rastering the primary beam across areas measuring 5x5 µm with 25% blanking, and 3x3 µm for smaller grains, collecting 100 measurement cycles (10 blocks, 10 measurements per block). Secondary ion beam and EOS centering were automatically conducted at the beginning and end of each analysis. All sample analyses were bracketed by analyses of the in-house SON-3 pyrite standard (see Farquhar et al., 2013 for details of the standard).

Yield, dead-time and background corrected $^{34}S/^{32}S$ raw ratios (R_{raw}) were drift corrected using a linear regression:

$$R_{drift} = R_{raw} - mx \tag{1}$$

where m is the slope of the regression and x is the analysis number for the session, scaled to ensure that the intercept (c) crosses the x-axis at x = 0. The drift corrected ratios were expressed as raw delta values (V-CDT) using:

$$\delta^{34}S_{drift} = 1000 \left(\frac{R_{drift}}{0.0450045} - 1 \right) \tag{2}$$

Instrumental mass fractionation (α) was then calculated as the σ_{drift}^{-2} weighted average of all estimates α_i of the $\delta^{34}S_{drift}$ values for the bracketing standards:

$$a_i = \frac{1 + \delta^{34}S_{drift}/1000}{1 + \delta^{34}S_{std}/1000} \tag{3}$$

where $\delta^{34}S_{std}$ is the $\delta^{34}S_{\text{V-CDT}}$ of the SON-3 pyrite standard (+1.61 ± 0.08 ‰). Finally, single sample analyses were corrected to V-CDT using:

$$\delta^{34}S_{sample} = \left[\left(1 + \frac{\delta^{34}S_{drift}}{1000} \right) / a - 1 \right] * 1000 \tag{4}$$

Error propagation followed the protocol outlined in McLoughlin et al. (2012) and includes uncertainties associated with instrumental precision, drift correction, and the reference value for the SON-3 standard. Correction for quasi simultaneous arrivals is not required when a Faraday Cup rather than an electron multiplier is used to detect the more abundant ^{32}S isotope. All samples were confirmed as pyrite using laser Raman micro-spectroscopy and EDS so no corrections for matrix effects between the samples and our SON-3 pyrite standard were required. Post analysis, all analysis craters were checked to ensure that they were entirely within pyrite grains and no non-pyritic matrix had been included in the sputtering process. All analyses were completed in a single analytical session and the uncertainty on bracketing $\delta^{34}S$ standard analyses for this session was 1.3 ‰ (n = 19). Propagated errors for individual analyses (1σ) are listed in the final column of Table 1.

Laser Raman microspectroscopy

Confocal laser Raman microspectroscopy was performed on a *WITec alpha 300RA+* instrument with a *Toptica Photonics Xtra II* 785 nm laser source at CMCA. The laser was focused through either a 20x/0.4, 50x/0.5 or 100x/0.9 objective, the latter obtaining a spot size of smaller than 1 μm, and the laser excitation intensity at the sample surface was in the 1-5 mW range. Spectral acquisitions were obtained with 600 l/mm grating and a peltier-cooled (-60 °C) 1024 x 128 pixel CCD detector. Laser

centering and spectral calibration were performed daily on a silicon chip with characteristic Si Raman band of 520.4 cm^{-1}. Count rates were optimised prior to point spectra acquisition or hyperspectral mapping using the dominant quartz Raman band of 465 cm^{-1}. Spectra were collected in the 100-1800 rel. cm^{-1} region in order that both 1st order mineral vibration modes and 1st order carbonaceous vibration modes could be examined simultaneously. Raman maps were acquired with the spectral centre of the detector adjusted to 944 cm^{-1}, with a motorised stage allowing XYZ displacement with precision of better than 1 μm. Spectral decomposition and subsequent image processing were performed using WITec Project FOUR software, with baseline subtraction using a 3rd or 4th order polynomial. Carbon maps were created by integrating over the ~1600 cm^{-1} 'G' Raman band, quartz maps using the ~ 465 cm^{-1} Raman quartz peak and chlorite maps using ~680 cm^{-1} (and confirmed by the 550 cm^{-1}) Raman chlorite peak. All analyses were conducted on material embedded below the surface of the thin section to avoid artefacts in the Raman spectra resulting from polishing and/or surface contamination.

RESULTS

Sample overview and mineralogy

The new occurrence of AITs is found in the 1878 Ma Gunflint Formation (Fralick et al., 2002), at the Current River Locality, north of Boulevard Lake, Thunder Bay, Ontario (grid reference N 48°28'08", W 089°12'04"). The AITs occur in a ferruginous phosphatic chert-carbonate (Fig. 2), bedding surfaces of which show microbially induced sedimentary structures (MISS) including wrinkle mats (Fig. 2a) and irregular craters suggestive of collapsed biosedimentary domes in microbial mats (Fig. 2b). The ~60 cm thick unit is composed of two main types of sediment: a very

fine-grained ferruginous organic-rich chert; and a coarser iron carbonate, with the chert component predominating (McMahon, 2010). Towards the top of the unit, pyrite and organic material forms conspicuous wavy laminae intercalated with granular phosphate (Fig. 2c). Irregular chert-filled cavities are also common at this level (Fig. 2c). These cavities closely resemble, and are here interpreted as, birds-eye fenestrae formed by gas entrapment within the sediment. Fenestrae are particularly common in microbial carbonate sediments where they are caused by the decay of voluminous organic material; they may also be caused by the drying out of microbial mats resulting in shrinkage and the lifting of part of the mat away from the underlying sediment (Flugel, 2004). Silicified crusts and rip-up clasts indicate that silicification was likely syn-depositional (Simonson, 1987; Pufahl and Fralick, 2000). AITs are found in the chert-filled fenestrae, most commonly at the edges of fenestrae bordered by pyrite, chlorite and organic material, and more rarely enclosed within fenestrae where they often radiate away from patches of chlorite. Elemental mapping of a transect through a fenestra confirms a relatively pure micro-quartz (chert) composition (Fig. 2d, orange), plus numerous tiny pyrite grains (Fig. 2d, pink) and patches of Mg-Fe-rich silicate minerals (Fig. 2d, green; chlorite, see below for identification). The fenestra is enclosed by the pyrite- and chlorite-rich sediment and clusters of pyrite are observed along the margins of the fenestra; underlying granular phosphate (Fig. 2d, blue) also contains significant pyrite but no fenestrae.

Previous reports of AITs from the Gunflint Formation (Tyler and Barghoorn, 1963; Knoll and Barghoorn, 1974) contain little locality information but the AITs therein differ in morphology and infilling mineralogy to those described here, and are shown to occur in close proximity to ooids. Hence, we infer that they come from oolitic

cherts at the Schreiber locality in the lower member of the Gunflint Formation
(samples that Tyler and Barghoorn investigated in some detail in the 1950's and
1960's), some 150 km to the east of our sample.

AIT morphology and distribution

Microtubular structures are found in multiple chert-filled fenestrae within a pyrite-rich
microbial mat (Figs. 3-5). These microtubes are here classified as AITs due to the
frequent occurrence of terminal pyrite grains (Figs. 3a-c, 4c-d), occasional
longitudinal striations along the microtubes (Fig. 4a), polygonal cross sections (see
Fig. 8 below), and close comparison to previously reported AITs in Precambrian
rocks (cf. Wacey et al., 2008b). The AITs range in diameter from ~1 μm up to 15 μm
and can be 200 μm or more in length, though most are in the 20-100 μm range (Figs.
3-5). They have a wide range of morphologies from almost straight (e.g., Fig. 4b, d),
to gently curved (e.g., Figs. 3b, 4e), twisted in multiple directions (e.g., Figs. 3a, 4a),
and tightly coiled (e.g., Figs. 3c, 4c). A number of examples have both a terminal
pyrite grain and fragments of pyrite scattered further back within the microtube (Fig.
4c). Some AITs also have particularly dark walls that may indicate further
concentrations of nano-grains of pyrite or organic material (Fig. 4e). Most AITs have
a continuous, rather homogenous mineral infill, but rare examples exhibit a
segmented habit (Fig. 4b, arrow).

The presence and quantity of AITs in a given chert fenestra is highly variable. Some
fenestrae have hundreds of AITs enclosed within, while others may have single figure
occurrences or none at all. The size of the fenestra does not appear to be a primary
controlling factor here, though clearly there is more volume for a greater number of

AITs in larger fenestrae. Rather, it appears that the abundance of pyrite (and potentially also organic material and chlorite) along the boundary of the fenestra is the primary factor in controlling AIT numbers; this is evidenced in some fenestrae by the concentration of AITs along only the boundary edges that are particularly dark and pyrite-rich (e.g., Fig. 3a-b). This pattern is complicated within some fenestrae by significant patches of chlorite, in which numerous AITs are rooted and radiate away into chert (Figs. 3d, 4b). Not all patches of chlorite are foci for AITs; those that are appear rather dark in nature and show some evidence for residual dark brown organic material and/or pyrite (Fig. 3d-e).

Microtubular structures also occur entirely within some patches of chlorite (Figs. 3e, 4d). Identification of these as *bona fide* AITs is complicated by their rare occurrence and, hence, lack of defining morphological characteristics. In addition, platy chlorite crystals viewed in cross section can superficially resemble AITs, though these crystals are generally sub-micron in size and are pointed at both ends. In spite of these difficulties, the presence of a terminal pyrite crystal in one occurrence of a microtube within chlorite (Fig. 4d) and their strong morphological resemblance to AITs nearby in the chert, lead us to interpret these microtubes as AITs. These AITs occur at the boundary between chlorite patches and chert within the fenestrae and do not cross this boundary (Figs. 3e, 4d). The single example with a terminal pyrite grain serves as evidence that pyrite propulsion was into the chlorite from the chert-chlorite boundary (Fig. 4d), although we cannot be certain that this is the case for all such examples.

Geochemistry of AITs

Organic material

Laser Raman micro-spectroscopy combined with TEM revealed the nature and distribution of carbon in and around the AITs. Raman spectra show well developed carbon 'D' and carbon 'G' peaks at ~1350 cm^{-1} and ~1600 cm^{-1} respectively that are characteristic of organic kerogenous carbon (Supp. Fig. 1). The width, position and relative intensities of these peaks are consistent with kerogen of moderate thermal maturity (Wopenka and Pasteris, 1993; Yui et al., 1996) that has undergone the prehnite-pumpellyite to lower greenschist facies metamorphic heating experienced by these Gunflint rocks (Gross, 1964; Pufahl et al., 2000). Hence, the carbon is not a modern contaminant phase. Organic carbon is common both at the edges of the fenestrae (Fig. 5c) and within patches of chlorite interior to the fenestrae (Fig. 5b, d), concentrated in zones that serve as the points of initiation for many of the AITs. Carbon also occurs within individual AIT microtubes; here, the quantity of carbon is quite variable, ranging from rare, isolated blebs at the outer margin of a microtube (Fig. 5d-e) to more coherent masses infilling parts of the microtube or concentrated along microtube walls (Fig. 5b). Some AITs do not appear to have any carbon closely associated with them (Fig. 5a). However, entire AITs are rarely found within the plane of the thin section so it is not possible to be sure whether carbon is completely absent from any AITs. Two AITs were examined at higher spatial resolution using TEM (Figs. 6-8); very minor amounts of carbon were detected along the edge of a propelled pyrite grain (Fig. 7f) but no enrichment of carbon was seen along AIT walls (Figs. 7-8).

Elemental and mineralogical analysis

All studied examples of AITs appear to have minerals infilling their tubular appendages. In petrographic thin sections these minerals range in colour from very

16

pale green to pale brown and olive green (Figs. 3-5). We have characterised the minerals from two AIT appendages at the nano-scale (Figs. 6-8) using transmission electron microscopy (TEM). Figure 6 shows part of a propelled grain (dark grey) sitting at the terminal end of a microtube that is infilled by a mineral (medium grey) whose chemical composition is clearly different to the quartz matrix (light grey) through which the grain has been propelled. Elemental mapping in the TEM shows that the propelled grain is pyrite and the mineral infilling the microtube is an iron- and magnesium-rich aluminosilicate (Fig. 7). The proportions of Fe, Mg in the aluminosilicate are spatially variable. Analysis of a second AIT microtube (Fig. 8; note that the terminal pyrite grain is out of the plane of view on this occasion) again reveals a Fe-Mg-aluminosilicate as the infilling mineral phase, and emphasizes the polygonal cross sectional morphology of the microtube. The proportions of Fe and Mg are again somewhat variable with Fe-rich grains restricted to the upper right hand domain of the microtube (Fig. 8f arrow). The bright-field TEM image (Fig. 8a) shows that the microtube infill comprises multiple sheet-like aluminosilicate grains, aligned approximately parallel to the sides of the microtube. The morphology of these grains suggests a phyllosilicate mineral and this is confirmed by selected area electron diffraction (SAED) in the TEM (Fig. 8b). These data show a series of arcs, with the arcs nearest the centre of the pattern representative of a set of closely aligned 2:1 phyllosilicate crystals viewed along the <100> zone axis. The d-spacings of 1.42 nm, and 0.46 nm match the {001} plane and {020} plane respectively of a monoclinic chlorite (Zanazzi et al., 2007). This, together with the variable elemental chemistry suggests that the minerals infilling the microtubes are a mixture of chlorites from the clinochlore (Mg-rich) to chamosite (Fe-rich) solid solution series (Deer et al., 2009). Laser Raman analysis of fifteen further AITs (e.g., Fig. 5) provided corroboration of

the overall chloritic mineralogy of the microtubular appendages, with dominant

Raman peaks at ~550 cm^{-1}, ~680 cm^{-1} and 355 cm^{-1} (cf. RUFF database ID R060725;

http://rruff.info/clinochlore/display=default/R060725), and also confirmed that the

fenestral matrix was quartz.

Isotopic analysis

Propelled pyrite grains within some of the larger AITs, plus pyrite bordering the

chert-filled fenestrae were analysed *in situ* for their sulfur isotope composition using

NanoSIMS (Table 1; Fig. 9). Twenty one pyrite grains were analysed and these have a

range of $\delta^{34}S_{V\text{-CDT}}$ values from -8.5 ‰ to +8 ‰ (mean = -0.1 ‰; n=21). Uncertainties

on individual data points are between 0.6 ‰ and 1.5 ‰ (1σ). The most negative

values equate to a maximum fractionation of around 30 ‰ from Palaeoproterozoic

seawater sulfate ($\delta^{34}S_{V\text{-CDT}}$ = +20 ‰ +/- 2 ‰; Canfield and Raiswell, 1999).

DISCUSSION

This is the first report of AITs from within a microbial mat and the first report of $\delta^{34}S$

data directly from pyrite grains within AITs, allowing the mechanism of formation of

the propelled pyrite grain to be tested and evaluated. We first discuss potential pyrite

formation mechanisms and then go on to discuss possible formation mechanisms and

timing for the AITs.

Pyrite formation mechanism

The sulfur isotope data, together with the observed mineral assemblage and

interpreted geological setting, can be used to determine possible pyrite formation

mechanisms. One such mechanism is pyrite formation via microbial sulfate reduction

(MSR). During MSR, the lighter ^{32}S isotope is more rapidly reduced than ^{34}S (e.g., Kaplan and Rittenberg, 1964). Hence, dissolved sulfide becomes enriched in ^{32}S and this is incorporated into early-formed pyrite. If the site of pyrite formation remains open to the sulfate source then the resultant pyrite will have a narrow range of rather light $\delta^{34}S$ values. The exact magnitude of the fractionation will be dependent on factors such as sulfate concentration (Habicht et al., 2002), sulfate reduction rate (Chambers et al., 1975), supply of electron donors reflecting to the type and quantity of organic material present (Sim et al., 2011, 2012), and species of sulfate reducing bacterium (Detmers et al., 2001), but it is the narrow range of $\delta^{34}S_{pyrite}$ that typically characterizes an open system (e.g., Faure, 1986). In contrast, if the pore-waters become isolated from the overlying seawater sulfate source, the residual pore-water sulfate becomes progressively enriched in ^{34}S as MSR proceeds (cf. Wacey et al., 2007) and leads to later-formed pyrite with heavier $\delta^{34}S$ signatures. Following this model, our $\delta^{34}S_{pyrite}$ range of -8.5 ‰ to +8 ‰ would suggest that MSR was initially taking place within microbial mat porewaters open to moderate concentrations of seawater sulfate (cf. Rickard et al., 2007), and with MSR fractionation factors up to 30 ‰. This quickly could have evolved to a state of sulfate limitation due to low porosity in the microbial mat supplemented by occlusion of pore-space by contemporaneous silicification, and would have resulted in the variable $\delta^{34}S$ values observed here.

The sulfur isotope data are not, however, uniquely attributable to MSR. Most abiotic pyrite-forming mechanisms result in $\delta^{34}S_{pyrite}$ values that are less variable and cluster closer to 0 ‰ than those observed herein (e.g., Seal, 2006) but there are exceptions. For example, sulfides precipitated in epithermal hydrothermal systems can show a

range in $\delta^{34}S$ from about -7 ‰ to +7 ‰ (Seal, 2006), H_2S emanating from seafloor hydrothermal systems has been reported to be as negative as -5.7 ‰ (Gamo et al., 1997), and some sulfides from such deposits as heavy as +8.3 ‰ (Alt and Chaussidon, 1989). Furthermore, pyrite precipitated hydrothermally in veins within Martian meteorites has been reported to have $\delta^{34}S$ extremes of -6.1 ‰ (Greenwood et al., 2000) and +7.8 ‰ (Shearer et al., 1996). Hence, an alternative explanation could be that the AIT pyrite has a hydrothermal source, since the Animikie basin was tectonically and volcanically active during deposition of the Gunflint Formation, evidenced by minor mafic flows (Goodwin, 1956) and extensive tuffaceous horizons (Fralick et al., 2002).

An additional complication in the interpretation of our $\delta^{34}S$ data is caused by the scale at which the analyses were performed. Most previous sulfur isotope data have come from bulk rock or bulk fluid measurements (i.e. millimeter to centimeter scale). In comparison, our data come from the micrometer to millimeter scale. While (Nano)SIMS has the advantage of being able to detect spatial variations in isotopic data that were previously unresolvable, and is the only way in which <15 μm diameter pyrites within AIT could be analysed, it is a relatively new technological advance and there are limited datasets that can serve as reference points for data interpretation. This problem is highlighted when the mean value of our data is considered ($\delta^{34}S_{pyrite} = -0.1‰$; n=21). A traditional bulk isotopic analysis from this sample may have only resulted in a single data point close to this mean value, leading to an interpretation that the pyrite formed from fluids derived from a purely magmatic/hydrothermal source ($\delta^{34}S = 0.3$ ‰ +/-0.5 ‰; Sakai et al., 1984). Furthermore, twenty-one spot analyses may not be representative of the bulk pyrite within this rock, serving to

further complicate subsequent interpretations.

Nevertheless, our interpreted formation mechanism for the AIT pyrite is via MSR, for the following reasons. Firstly, the isotopic data, having a spread of 16.5 ‰, are entirely consistent with the model of MSR operating in conditions evolving to sulfate limitation described above. Secondly, such a spread in $\delta^{34}S_{pyrite}$ values over small spatial scales compares well with other recent NanoSIMS data from the Gunflint Formation, where pyritised microfossils from the stromatolitic Schreiber Beach locality have a 15 ‰ spread in $\delta^{34}S_{pyrite}$ over spatial scales of only a few millimeters (Wacey et al., 2013). Those data ($\delta^{34}S_{V-CDT}$ of 6.7 ‰ to 21.5 ‰) were interpreted as indicative of a pyrite forming via MSR in a system initially open to seawater sulfate but rapidly evolving to sulfate limitation due to early silicification (Wacey et al., 2013). In contrast, a hydrothermal fluid is unlikely to have such variable $\delta^{34}S$ on the micrometer to millimeter scale, although we acknowledge that this is not impossible. For example, Alt and Chaussidon (1989) reported just over a 12 ‰ variation in $\delta^{34}S$ at the millimeter to centimeter scale between and within hydrothermal sulfides from the Costa Rica Rift; further analyses of abiogenic sulfides by (Nano)SIMS are required in order to fully understand the isotopic variability possible at this scale. Thirdly, the geological setting within a microbial mat combined with a biosedimentary mineral assemblage of phosphate, carbonate and pyrite is more consistent with a MSR model than with an abiogenic hydrothermal model of pyrite formation.

Potential AIT formation mechanisms

The data and discussion presented above suggest that the pyrite grains within the AITs were formed via the activity of sulfate reducing bacteria. We now go on to

discuss the potential mechanisms by which these pyrite grains were propelled through the chert fenestrae to form the AITs, plus the relative timing of these events.

A biologically-mediated mechanism has previously been invoked for the propulsion of some pyrite crystals to create AITs (e.g., Knoll and Barghoorn, 1974; Wacey et al., 2008a, b). This has largely been based upon the presence of organic material in and around the AITs. Organic material has been reported at the terminal end of AITs (Knoll and Berghoorn, 1963; Lepot et al., 2009), along AIT walls (Wacey et al., 2008b), or disseminated within AIT microtubes (Wacey et al., 2008a; Lepot et al., 2011). Organic material also commonly occurs as patches/clots from which AIT microtubes radiate away (Knoll and Barghoorn, 1974; Buick, 1990; Wacey et al., 2008a; Tiwari and Siddaiah, 2012), or more generally in close proximity to the origin of an AIT microtube (Lepot et al., 2011). In addition, some AITs occur in micro-environments where plentiful biological material would have initially been present, for example in animal embryos (Xiao and Knoll, 1999), in fish scales (Wacey et al., 2008a), or in crustacean body cavities (Olempska and Wacey, 2016). However, some AIT occur in lithologies where biology is unlikely to have been present and in these cases it must be assumed that any organic material was of abiotic origin (e.g., Lepot et al., 2009, 2011), and there are also rare cases where organic material is not observed associated with AITs (McLoughlin et al., 2013).

This new suite of Gunflint Current River AITs occur within a microbial mat, are frequently associated with organic carbon, and contain pyrite interpreted to have formed via the action of sulfate reducing bacteria. The distribution of organic material shows some minor differences to that reported previously for AITs. It most commonly

occurs at the margins of the fenestrae close to the origins of many AITs, and on a few occasions as small clumps within AITs. Previous observations showing organic carbon enrichment in narrow zones along AIT walls (e.g., Wacey et al., 2008a) are only rarely repeated here, while reports of organic material on the leading edge of terminal grains (Barghoorn and Tyler, 1963) are not confirmed here. This could suggest that a larger volume of organic material was attached to pyrite grains in those previous settings. Alternatively, those previous observations could reflect passive accumulation of organics as the pyrite crystal was propelled through a chert matrix already rich in organic matter. This latter explanation is supported by reports that longer AITs had thicker organic films on the leading edge of the propelled pyrite crystal (Tyler and Barghoorn, 1963).

In the Current River microbial mats we propose that AIT formation commences with pyrite precipitation via the action of heterotrophic sulfate-reducing bacteria (SRB) decomposing preformed organic material. Sulfur isotope data suggest that this process was syngenetic to very early diagenetic, occurring within the microbial mat as porewaters were becoming isolated from overlying seawater and hence depleted in seawater sulfate. The activity of SRB (and potentially other anaerobes) would have produced gaseous products such as CO_2 that may have helped to produce the characteristic birds-eye fenestral fabrics now observed in thin section. Contemporaneous silicification of Gunflint sediments (cf. Simonson, 1987) would have resulted in silica precipitation in pore spaces, in particular within the fenestrae, further reducing porosity.

It is possible that these metabolic gases provided the propulsive force for the movement of newly formed pyrite crystals at a syngenetic to early diagenetic stage (cf. Zhang et al., 2015). However, there are potential problems with such a model. For example, it is difficult to conceive how sufficient gas pressure can build up in a microenvironment that supports active metabolism. A build up in gas pressure requires the closure of porosity, but such a closure is highly likely to cease metabolism due to exclusion of nutrients and accumulation of toxic waste products. In addition, the ferruginous nature of Gunflint samples suggests that Fe^{2+} was not limiting and so H_2S would likely have reacted with aqueous Fe^{2+} to form pyrite, while CO_2 could have dissolved in residual water and formed carbonates (which are readily observed in surrounding Gunflint sediments). Hence, AIT formation is unlikely to have occurred during this syngenetic to early diagenetic phase.

Previous models of AIT formation (e.g., Knoll and Barghoorn, 1974) have suggested that AITs are formed rather later in the diagenetic (or metamorphic) history of the rock, largely initiated by heating and thermal decomposition of residual organic material. Such thermal decomposition of organic material produces gases (e.g., CO_2, CH_4) that in turn lead to localized pressure build up in a rock matrix whose porosity is now completely closed. This provides the propulsive power to move crystals of higher hardness and lower solubility through a more soluble matrix, via a pressure-solution process (Knoll and Barghoorn, 1974). In this model, the organic material may aid the dissolution of the quartz rock matrix by providing a localized build-up of organic acids around the propelled crystal; this may increase the dissolution rate of quartz by up to ten times compared with pure water, even at low temperatures (Bennett et al., 1988). This formation mechanism is largely consistent with observations from the

Current River AITs described here. However, the ubiquitous presence of chlorite at fenestra margins, the infilling of AITs by chlorite, plus the observation of AITs originating at patches of chlorite encased within fenestrae (e.g., Figs. 3d, 4b) deserves further consideration, and leads us to suggest an additional contributing factor to AIT formation in this setting.

This additional mechanism involves mineral phase change reactions during burial diagenesis and low grade metamorphism. A number of possible reactions may account for the formation of chlorite in fine-grained sediments during diagenesis and low-grade metamorphism. These include: the alteration of Fe-rich clay minerals such as berthierine; the alteration of mafic minerals such as biotite; progressive reaction of smectites via corensite to chlorite; as a by-product of the smectite to illite reaction; via the breakdown of kaolinite; and via reactions of dioctahedral clays with carbonates (e.g., Hurst, 1985; Hillier, 2003). Some of these reactions lead to a fluid volume increase due to the release of water. For example, there is a 5-10 % volume increase during the transformation of smectite to illite (Bjørlykke, 1993), that could potentially increase local fluid pressures in an impermeable sediment, help provide a mechanism for pyrite movement, and maintain the necessary aqueous film around the pyrite for pressure dissolution of the matrix. Other chlorite-forming reactions produce CO_2 as a by-product, for example the reaction of dolomite or ankerite with kaolinite or illite (e.g., Muffler and White, 1969; Hutcheon et al., 1980). This reaction may occur at temperatures as low as 120°C (Hillier, 1993), well within the range of temperatures experienced by these rocks, and produce relatively large quantities of CO_2. Hillier (1993) calculated that reaction of 20 wt% dolomite to form chlorite would produce approximately 1 mole of CO_2 per kilogram of rock – roughly 10 times the CO_2

produced by decarboxylation of organic matter in organic rich shales (Bjørlykke, 1988). Localised trapping of CO_2 released from such chlorite forming reactions could then drive AIT formation, consistent with the observed pattern of AIT radiating away from patches of chlorite.

The question of why pyrite grains appear to have been propelled from a softer material (clay/chlorite) into a harder material (quartz) also requires discussion. A number of geological field studies have found that the presence of clay minerals enhances the dissolution of quartz (e.g., Fisher et al., 2000) and this has been corroborated by laboratory studies and numerical simulations (Dewers and Ortoleva, 1991). In this scenario, increased volumes of water, held either between the clay platelets, or between clay and quartz (due to relatively large hydration forces of clays) promote dissolution. In addition, the dissolution of the clays themselves may release certain cations that increase the solubility of adjacent quartz (Dove, 1999). Hence it is plausible that clay minerals were both a source of enhanced chemical dissolution of quartz and a key reactant for the formation of chlorite, which is now observed infilling the AITs and overprinting inferred clay-rich zones within and around the fenestrae. This 'chlorite-mediated' AIT formation mechanism is also consistent with a number of other observations including: the proximity of chlorite and carbonate in some previously reported AIT lithologies (Lepot et al., 2009, 2011); chlorite interpreted as a replacement of carbonate in some previously reported Gunflint AIT (Tyler and Barghoorn, 1963); and the occurrence of primary carbonate both locally (McMahon, 2010) and more generally (e.g., Sommers et al., 2000) in the Gunflint Formation. Furthermore, this formation mechanism provides a plausible explanation

for the presence of AITs in rocks that have experienced little or no biological input (Lepot et al., 2009, 2011; McLoughlin et al., 2013).

The exact timing of AIT formation at Current River is difficult to deduce with any certainty and there may have been more than one phase of crystal propulsion and more than one phase of chlorite growth. AITs could conceivably have begun forming as soon as silica had crystallised to an extent where localized regions in the vicinity of pyrite, clay and organic material became impermeable. However, the majority of AITs likely formed at elevated temperature where both thermal decomposition of organic material and clay mineral alteration to chlorite led to both increased fluid/gas pressure and enhanced chemical dissolution of quartz. The youngest AITs are probably those found entirely within chlorite (Figs. 3e, 4d); these appear to cross cut an early generation of chlorite (inferred to be crystalline at the time of AIT formation) and are infilled by further chlorite, though the time elapsed between these chlorite generations may not be long.

CONCLUSIONS

This contribution describes a new suite of ambient inclusion trails (AITs) from a pyrite- and phosphate-rich fossilized microbial mat at the Current River locality of the 1878 Ma Gunflint Formation, Thunder Bay, Ontario. The AITs occur in chert-filled birds-eye fenestrae within the microbial mat, are 1-15 μm in diameter and can be hundreds of micrometers in length. Those that terminate in the plane of the thin section have a pyrite grain at their distal end, and all have microtubular appendages filled with chlorite. Unique *in situ* sulfur isotope data from pyrite grains within AITs ($\delta^{34}S_{V\text{-}CDT}$ = -8.5 to +8.0 ‰) reveal that these grains were formed via microbial sulfate

reduction during early diagenesis. Thermal decomposition of organic material attached to pyrite grains during burial and low-grade metamorphism provided one potential propulsive force for AIT formation. A newly described occurrence of AIT radiating away from patches of chlorite, and sometimes confined entirely within the chlorite, suggests that mineral transitions (e.g., smectite to illite reaction and/or alteration of clay minerals and carbonate to chlorite) may provide sufficient localized increases in fluid/gas pressure and quartz dissolution rates to form AITs. At Current River it is likely that thermal decomposition of organics, plus chlorite formation, worked in tandem to form the AITs. However, the alteration of clay minerals to chlorite also provides a plausible single mechanism for the generation of AITs in organic-poor/abiotic environments.

ACKNOWLEDGEMENTS

The authors declare no conflicts of interest

REFERENCES

Alt JC, Chaussidon M (1989) Ion microprobe analyses of the sulfur isotopic compositions of sulphides in hydrothermally altered rocks, DSDP/ODP hole 504B. In: Becker K et al. *Proceedings of the Ocean Drilling Program, Scientific Results* **111**, 41–45.

Awramik SM, Schopf JW, Walter MR (1983) Filamentous fossil bacteria from the Archean of Western Australia. *Precambrian Research* **20**, 357–374.

Bennett PC, Melcer ME, Siegel DI, Hassett JP (1988) The dissolution of quartz in dilute aqueous solutions of organic acids at 25°C. *Geochimica et Cosmochimica Acta* **52**, 1521–1530.

Bjørlykke K (1993) Fluid flow in sedimentary basins. *Sedimentary Geology* **86**, 137–158.

Buick R (1990) Microfossil recognition in Archean rocks; an appraisal of spheroids and filaments from a 3500 m.y. old chert-barite unit at North Pole, Western Australia. *Palaios* **5**, 441–459.

Canfield DE, Raiswell R (1999) The evolution of the sulfur cycle. *American Journal of Science* **299**, 697–723.

Chambers LA, Trudinger PA, Smith JW, Burns MS (1975) Fractionation of sulfur isotopes by continuous cultures of *Desulfovibrio desulfuricans*. *Canadian Journal of Microbiology* **21**, 1602–1607.

Conway Morris S, Bengtson S (1994) Cambrian predators: possible evidence from boreholes. *Journal of Palaeontology* **68**, 1–23.

Deer WA, Howie RA, Zussman J (2009) Rock Forming Minerals (2nd edition), The Geological Society of London.

Detmers J, Brüchert V, Habicht KS, Kuever J (2001) Diversity of sulfur isotope fractionations by sulphate-reducing prokaryotes. *Applied Environmental Microbiology* **67**, 888–894.

Dewers T, Ortoleva P (1991) Influences of clay minerals on sandstone cementation and pressure solution. *Geology* **19**, 1045–1048.

Dove PM (1999) The dissolution kinetics of quartz in aqueous mixed cation solutions. *Geochimica et Cosmochimica Acta* **63**, 3715–3727.

Farquhar J, Cliff J, Zerkle AL, Kamyshny A, Poulton SW, Claire M, Adams D, Harms B (2013) Pathways for Neoarchean pyrite formation constrained by mass-independent sulfur isotopes. *Proceedings of the National Academy of Sciences USA* **110**, 17638–17643.

Faure G (1986) Principles of Isotope Geology (2nd edition). John Wiley & Sons, New York, 589pp.

Fisher QJ, Knipe R, Worden RH (2000) Microstructures of deformed and non-deformed sandstones from the North Sea: implications for the origins of quartz cement in sandstone. In: Worden RH, Morad S (eds) Quartz Cementation in Sandstones. *Special Publication of the International Association of Sedimentologists* **29**, Blackwell Science, Oxford, pp.129–146.

Flugel F (2004) Microfacies of Carbonate Rocks, Springer, Berlin.

Fralick P, Davis DW, Kissin SA (2002) The age of the Gunflint Formation, Ontario, Canada: single zircon U-Pb age determinations from reworked volcanic ash. *Canadian Journal of Earth Science* **39**, 1085–1091.

Gamo T, Okamura K, Charlou J-L, Urabe T, Auzende J-M, Ishibashi J, Shitashima K, Chiba H (1997) Acidic and sulfate-rich hydrothermal fluids from the Manus back-arc basin, Papua New Guinea. *Geology* **25**, 139–142.

Greenwood JP, Riciputi LR, McSween HY Jr, Taylor LA (2000) Modified sulfur isotope compositions of sulphides in the nakhlites and Chassigny. *Geochimica et Cosmochimica Acta* **64**, 1121–1131.

Grey K (1986) Problematic microstructures in the Proterozoic Discovery Chert, Bangemall Group, Western Australia. Ambient grains or microfossils? Western Australian Geological Survey Record, ISSN 0508-4741.

Goodwin AM (1956) Facies relations in the Gunflint Iron Formation. *Economic Geology* **51**, 565–595.

Gross, G.A. (1965) Geology of iron deposits in Canada, volume I, general geology and evaluation of iron deposits. *Geological Survey of Canada, Economic Geology Report* **22**, 181p.

Gruner JW (1923) Algae, believed to be Archean. *Journal of Geology* **31**, 146–148.

Habicht KS, Gade M, Thamdrup B, Berg P, Canfield DE (2002) Calibration of sulphate levels in the Archean ocean. *Science* **298**, 2372–2374.

Hillier S (1993) Origin, diagenesis and mineralogy of chlorite minerals in Devonian lacustrine mudrocks, Orcadian Basin, Scotland. *Clays and Clay Minerals* **41**, 240–259.

Hillier S (2003) Chlorite in sediments. In: Middleton GV, Church MJ, Coniglio M, Hardie LA, Longstaffe FJ (Eds) Encyclopeadia of Sediments and Sedimentary Rocks, Kluwer, Dordrecht.

Hurst A (1985) Diagenetic chlorite formation in some Mesozoic shales from the Sleipner area of the North Sea. *Clay Minerals* **20**, 69–79.

Hutcheon I, Oldershaw A, Ghent ED (1980) Diagenesis of Cretaceous sandstones of the Kootenay Formation at Elk Valley (southeast British Columbia) and Mt. Allan (southwestern Alberta). *Geochimica et Cosmochimica Acta* **44**, 1425–1435.

Kaplan IR, Rittenberg SC (1964) Microbiological fractionation of sulphur isotopes. *Journal of General Microbiology* **34**, 195–212.

Knoll AH, Barghoorn ES (1974) Ambient pyrite in Precambrian chert: New evidence and a theory. *Proceedings of the National Academy of Sciences USA* **71**, 2329–2331.

Lepot K, Philippot P, Benzerara K, Wang G-Y (2009) Garnet-filled trails associated with carbonaceous matter mimicking microbial filaments in Archean basalt. *Geobiology* **7**, 393–402.

Lepot K, Benzerara K, Philippot P (2011) Biogenic versus metamorphic origins of diverse microtubes in 2.7 Gyr old volcanic ashes: Multi-scale investigations. *Earth and Planetary Science Letters* **312**, 37–47.

McLoughlin N, Brasier MD, Wacey D, Green OR, Perry RS (2007) On Biogenicity Criteria for Endolithic Microborings on Early Earth and Beyond. *Astrobiology* **7**, 10–26.

McLoughlin N, Staudigel H, Furnes H, Eickmann B, Ivarsson M (2010) Mechanisms of microtunelling in rock substrates: distinguishing endolithic biosignatures from abiotic microtunnels. *Geobiology* **8**, 245–255.

McLoughlin N, Grosch EG, Kilburn MR, Wacey D (2012) Sulfur isotope evidence for a Paleoarchean subseafloor biosphere, Barberton, South Africa. *Geology* **40**, 1031–1034.

McLoughlin N, Furnes H, Hanski EJ, Staudigel H (2013) Seeking textural evidence of a Palaeoproterozoic sub-seafloor biosphere in pillow lavas of the Pechenga greenstone belt. In: Melezhik V et al (eds) *Reading the Archive of Earth's Oxygenation: Volume 3: Global Events and the Fennoscandian Arctic Russia – Drilling Early Earth Project*, pp. 1371–1394.

McMahon S (2010) Deciphering a Palaeoproterozoic nutrient cycle: New evidence from phosphate in the 1.9-Ga Gunflint Formation, Canada. Oxford University Masters Thesis.

Muffler LJP, White DE (1969) Active metamorphism of upper Cenozoic sediments in the Salton Sea geothermal field and the Salton Trough, Southeast California. *Bulletin of the Geological Society of America* **80**, 157–182.

Olempska E, Wacey D (2016) Ambient inclusion trails in Palaeozoic crustaceans (Phosphatocopina and Ostracoda). *Palaeogeography, Palaeoclimatology, Palaeoecology* **441**, 949–958.

Pufahl P, Fralick P, Scott J (2000) Geology of the Paleoproterozoic Gunflint Formation. Institute on Lake Superior Geology Proceedings, 46th Annual Meeting, Thunder Bay, Ontario, 103–147.

Rickard D, Grimes S, Butler I, Oldroyd A, Davies KL (2007) Botanical constraints on pyrite formation. *Chemical Geology* **236**, 228–246.

Sakai H, Des Marais DJ, Ueda A, Moore JG (1984) Concentrations and isotope ratios of carbon, nitrogen, and sulfur in ocean-floor basalts. *Geochimica et Cosmochimica Acta* **48**, 2433–2442.

Schopf JW, Kudryavtsev AB, Agresti DG, Czaja AD, Wdowiak TJ (2005) Raman imagery: A new approach to assess the geochemical maturity and biogenicity of permineralized Precambrian fossils. *Astrobiology* **5**, 333–371.

Seal RR II (2006) Sulfur isotope geochemistry of sulphide minerals. *Reviews in Mineralogy and Geochemistry* **61**, 633–677.

She Z, Strother P, McMahon G, Nittler LR, Wang J, Zhang J, Sang L, Ma C, Papineau D (2013) Terminal Proterozoic cyanobacterial blooms and phosphogenesis documented by the Doushantuo granular phosphorites I: In situ micro-analysis of textures and composition. *Precambrian Research* **235**, 20–35.

Shearer CK, Layne GD, Papike JJ, Spilde NN (1996) Sulfur isotope systematics in alteration assemblages in Martian meteorite Allan Hills 84001. *Geochimica et Cosmochimica Acta* **60**, 2921–2926.

Sim MS, Bosak T, Ono S (2011) Large sulfur isotope fractionation does not require disproportionation. *Science* **333**, 74–77.

Sim MS, Ono S, Donovan K, Templer SP, Bosak T (2012) Effect of electron donors on the fractionation of sulfur isotopes by a marine *Desulfovibrio* sp. *Geochimica et Cosmochimica Acta* **75**, 4244–4259.

Simonson BM (1987) Early silica cementation and subsequent diagenesis in arenites from four Early Proterozoic iron formations of North America. *Journal of Sedimentary Petrology* **57**, 494–511.

Sommers MG, Awramik SM, Woo KS (2000) Evidence for initial calcite-aragonite composition of Lower Algal Chert Member ooids and stromatolites, Paleoproterozoic Gunflint Formation, Ontario, Canada. *Canadian Journal of Earth Science* **37**, 1229–1243.

Stockfors M, Peel JS (2005) Euendoliths and cryptoendoliths within late Middle Cambrian brachiopod shells from North Greenland. *GFF* **127**, 187–194.

Tiwari M, Siddaiah NS (2012) Ambient inclusion trails (AITs) from the Neoproterozoic Gangolihat Formation, Lesser Himalaya, India. *Palaeoworld* **21**, 92–

99.

Tyler SA, Barghoorn ES (1963) Ambient pyrite grains in Precambrian cherts. *American Journal of Science* **261**, 424–432.

Vernon RH (2004) *A Practical Guide to Rock Microstructures*, Cambridge University Press, Cambridge, UK.

Wacey D, Wright DT, Boyce AJ (2007) A stable isotope study of microbial dolomite formation in the Coorong region, South Australia. *Chemical Geology* **244**, 155–174.

Wacey D, Kilburn MR, Stoakes CA, Aggleton H, Brasier MD (2008a) Ambient inclusion trails: Their recognition, age range and applicability to early life on Earth. In: Dilek Y, Furnes H, Muehlenbachs K (Eds) *Links Between Geological Processes, Microbial Activities and Evolution of Life,* 113–134.

Wacey D, Kilburn MR, McLoughlin N, Parnell J, Stoakes CA, Brasier MD (2008b) Use of NanoSIMS in the search for early life on Earth: ambient inclusion trails in a c.3400 Ma sandstone. *Journal of the Geological Society of London* **165**, 43–53.

Wacey D, Menon S, Green L, Gerstmann D, Kong C, McLoughlin N, Saunders M, Brasier MD (2012) Taphonomy of very ancient microfossils from the ~3400 Ma Strelley Pool Formation and ~1900 Ma Gunflint Formation: new insights using focused ion beam. *Precambrian Research* **220-221**, 234–250.

Wacey D, Mcloughlin N, Kilburn MR, Saunders M, Cliff J, Kong C, Barley ME, Brasier MD (2013) Nano-scale analysis reveals differential heterotrophic consumption in the ~1.9 Ga Gunflint Chert. *Proceedings of the National Academy of Sciences USA* **110**, 8020–8024.

Wopenka B, Pasteris JD (1993) Structural characterization of kerogens to granulite-facies graphite: Applicability of Raman microprobe spectroscopy. *American Mineralogist* **78**, 533–557.

Xiao S, Knoll AH (1999) Fossil preservation in the Neoproterozoic Doushantuo phosphorite Lagerstätte, South China. *Lethaia* **32**, 219–240.

Xiao S, Hagadorn JW, Zhou C, Yuan X (2007) Rare helical fossils from the Doushantuo Lagerstätte: Ediacaran animal embryos come of age? *Geology* **35**, 115–118.

Yui T-F, Huang E, Xu J (1996) Raman spectrum of carbonaceous material: A possible metamorphic grade indicator for low-grade metamorphic rocks. *Journal of Metamorphic Geology* **14**, 115–124.

Zanazzi PF, Montagnoli M, Nazzareni S, Comodi P (2007) Structural effects of pressure on monoclinic chlorite: a single crystal study. *American Mineralogist* **92**, 655–661.

Zhang X, Pratt BR (2008) Microborings in Early Cambrian phosphatic and phosphatized fossils. *Palaeogeography Palaeoclimatology Palaeoecology* **267**, 185–195.
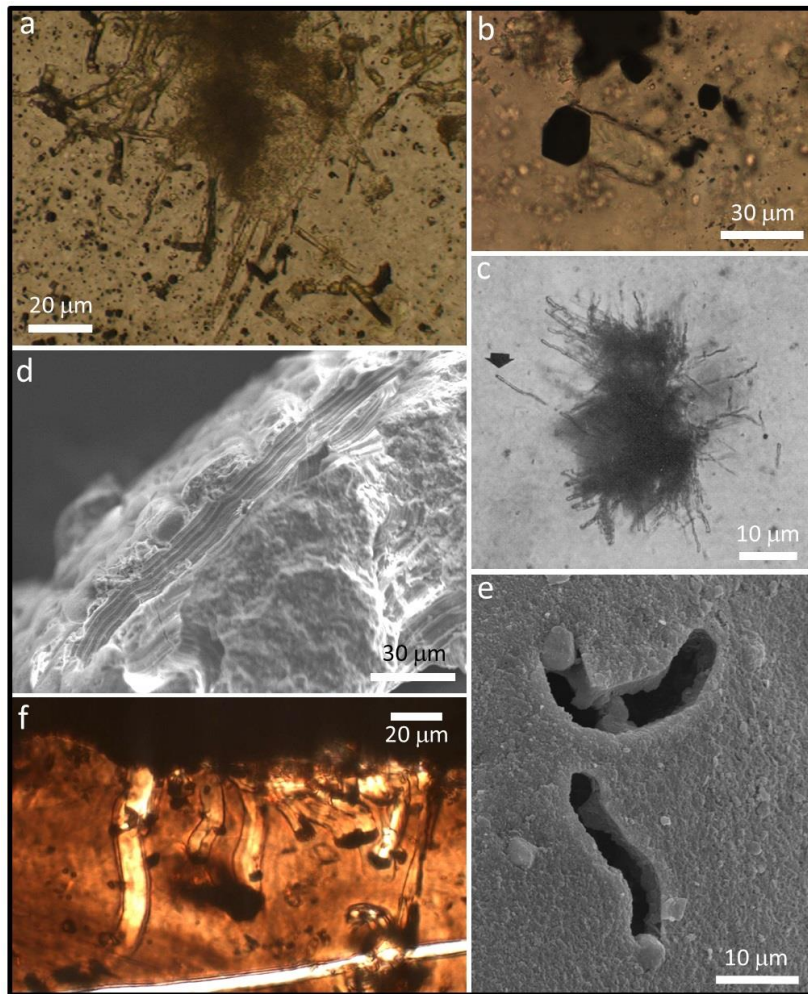
Figure 1. Characteristic morphology of AITs reported from the literature as context for this study. a) Multiple AITs infilled with jarosite and organic material from the ~3430 Ma Strelley Pool Formation, Western Australia. b) Single AIT with terminal pyrite crystal and infilled with chlorite from the ~3240 Ma Kangaroo Caves Formation, Western Australia. c) Multiple AITs arranged in starburst pattern radiating away from a clump of organic material, from the ~2700 Ma Fortescue Group, Western Australia. Arrow indicates terminal pyrite crystal (from Knoll and Barghoorn, 1974). d) Single open AIT on the surface of a phosphatic microfossil from the ~570 Ma Doushantuo Formation, China, showing longitudinal striations on the microtube wall. e) Two unfilled AITs with terminal pyrite crystals in a fossilised phosphatic crustacean valve from the early Devonian (~415 Ma) of the Ukraine. f) Multiple AITs, many with terminal pyrite crystals in a phosphatic fish scale from the Mid-Devonian (~390 Ma) Achanarras limestone of Scotland.

Figure 2. Lithology containing the AITs from the 1878 Ma Gunflint Formation, Current River locality, Thunder Bay, Ontario. Ferruginous phosphatic chert-carbonate with bedding surfaces showing (a) wrinkle structures and (b) craters indicative of collapsed biosedimentary domes, both of which point towards the former presence of a microbial mat. Finger and car key for scale respectively. (c) Scan of typical thin section through the AIT host lithology showing a wrinkled pyrite-rich microbial mat overlying a granular phosphate. AITs occur in the quartz-filled fenestrae (yellow arrows). d) Four colour element overlay map of the region shown by the green box in (c). Sulfur (pink) represents pyrite, magnesium (green) represents clay minerals (now chlorite; see Figs. 5, 7-8), calcium (blue) represents calcium phosphate, and silicon (orange) represents quartz (and clay minerals when co-occurring with Mg). This confirms that the quartz-filled fenestrae containing AITs are surrounded by a pyrite- and chlorite-rich sediment. Pyrite can be seen at the margins of the fenestra and small pyrite grains (pink dots), along with patches of chlorite, can also be seen within the fenestra. Pyrite is also common in the granular phosphate below suggesting that reducing conditions persisted throughout this depositional sequence. See Supplementary Fig. 2 for all of the individual element maps from this area. Scale bar is 200 μm.
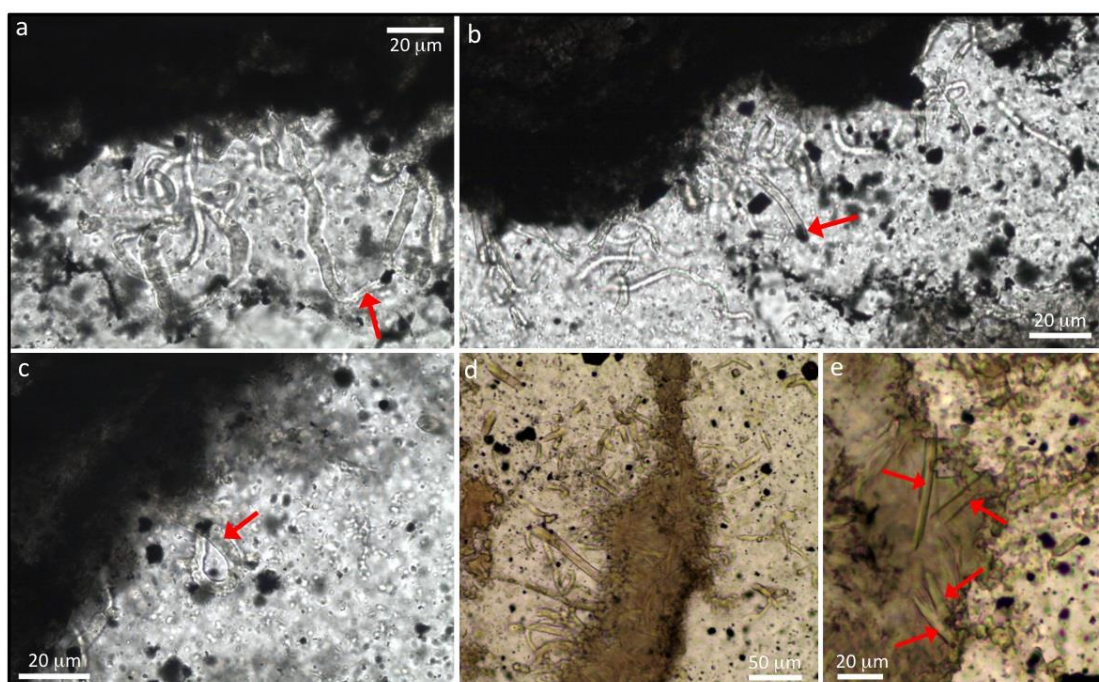
Figure 3. Petrographic overview of AITs from the Current River locality of the 1878 Ma Gunflint Formation. (a-c) Abundant AITs are found in fenestrae of clear microcrystalline quartz (chert) within microbial mats rich in pyrite. AIT can be almost straight, curved, twisted or spiral (arrow in c). AIT may take sudden changes of direction and can attain lengths of several hundred micrometers (arrowed example in a). Many have terminal pyrite crystals in the plane of the thin section (arrowed examples in a-c). d) Multiple AITs radiating away from a patch of chlorite within a chert-filled fenestra. E) Four putative AITs (arrows) occurring within a patch of chlorite that is itself within a chert-filled fenestra. An ultrathin section extracted from the AIT arrowed in (b) was examined using TEM (see Figs 6-7) and captured the boundaries between the terminal pyrite crystal, infilled microtube and quartz matrix.
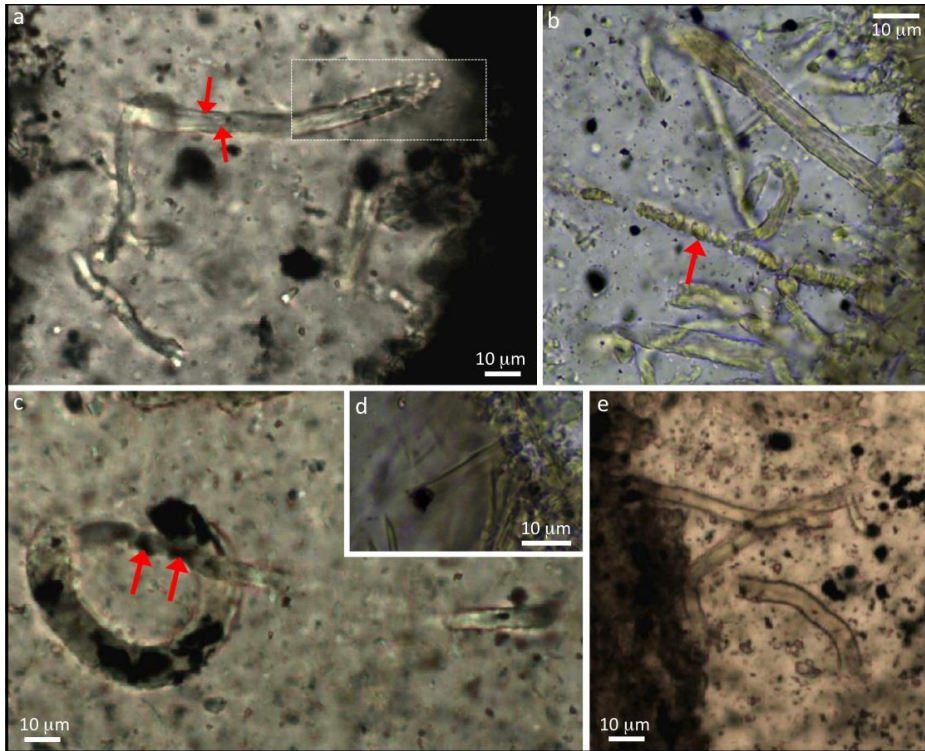
Figure 4. Detailed morphological features of AITs from the Current River locality. a) AIT with longitudinal striations (arrows) caused by movement of the propelled crystal through the silica matrix. The propelled crystal has moved out of the plane of view of the thin section. Note that boxed area is from a different focal plane to the rest of the image. b) Straight and gently curved AITs emanating from a zone of chlorite. Most AITs have a rather homogenous looking mineral infill at this spatial scale. The arrowed example, however, has a segmented morphology. c) A tightly curved AIT with a terminal pyrite grain and numerous fragments of pyrite within the microtube. A second, narrower AIT is seen cross cutting the first. It also has fragments of pyrite within it (arrows). d) An AIT within a patch of chlorite that exhibits a terminal pyrite grain. This appears to have been propelled away from the chlorite-chert boundary into the patch of chlorite. e) AITs with particularly dark longitudinal boundaries, suggestive of concentrations of carbon or pyrite along their margins.
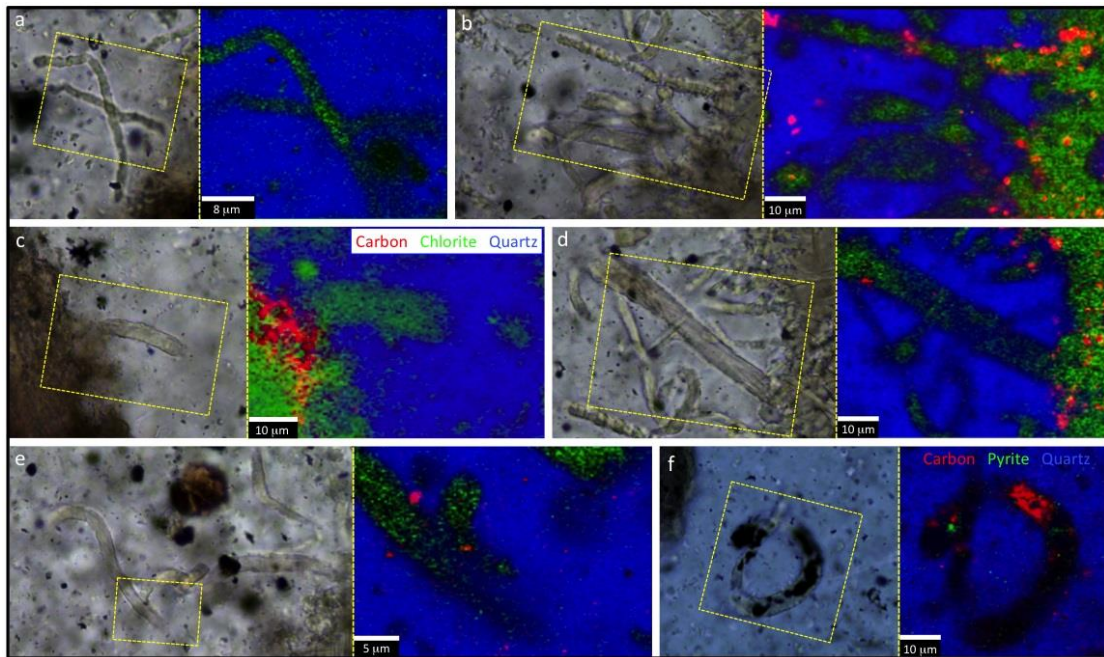
Figure 5. Distribution of organic material in relation to Gunflint AITs. Panels (a-e) each show a petrographic image of one or more AITs plus Raman data from the area indicated by the dashed yellow boxes. Each Raman image shows quartz (blue), chlorite (green) and carbon G (red) maps overlain on one another (see key in panel c), demonstrating that the AITs are infilled with chlorite, the matrix is quartz, and carbon occurs in close proximity to most AIT. Carbon is usually found close to where the AITs originate (b-d), although carbon can also be found in significant amounts (b) or minor amounts (d-e) further along the AIT, usually at their outer margins. However, not all AIT have carbon associated with them (a). (f) Petrographic image plus Raman map showing large quantity of carbon (red) within the AIT in close proximity to pyrite (green). Black areas in this panel are chlorite. Note the different colour key in this panel compared to panels (a-e).
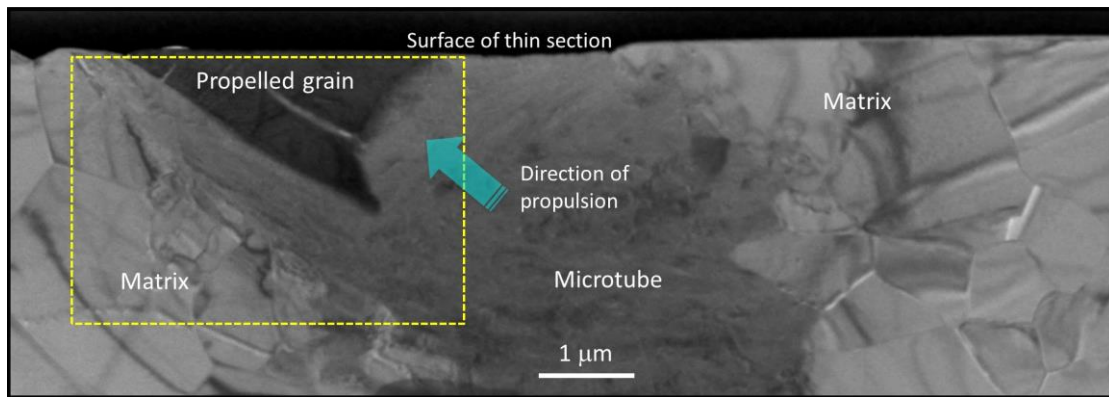
Figure 6. Bright-field TEM image of focused ion beam-milled ultrathin (~100 nm) wafer through the AIT indicated in Fig. 3b. This wafer captured part of the propelled mineral grain and part of the microtube, all set within a microcrystalline quartz matrix. Darker colours indicate higher atomic mass, hence the propelled grain has the highest mass, followed by the phase infilling the microtube, and finally the quartz matrix. The black band at the top of the image is the protective platinum strip deposited before cutting the wafer. Dashed box denotes area analysed in Fig. 7.
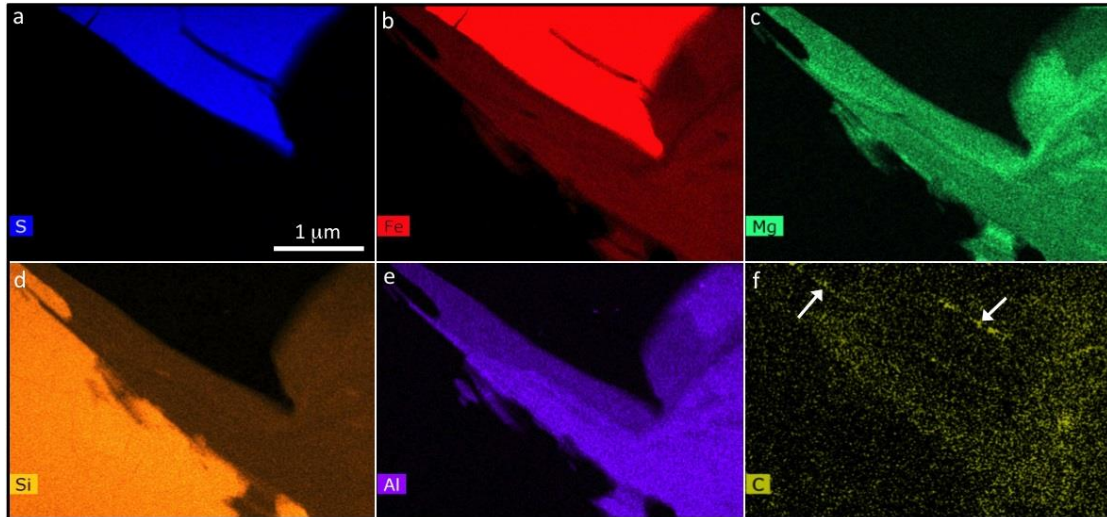
Figure 7. ChemiSTEM elemental maps of the boxed area indicated in Fig. 6.
Elemental mapping confirms the propelled crystal as pyrite and the matrix as quartz.
The microtube is infilled by an iron- and magnesium-rich aluminosilicate (see Fig. 8
for identification of this phase), where the proportions of iron and magnesium vary
across the microtube. There are minor accumulations of carbon along the edge of the
propelled pyrite crystal and within a fracture in the pyrite (arrows in f).
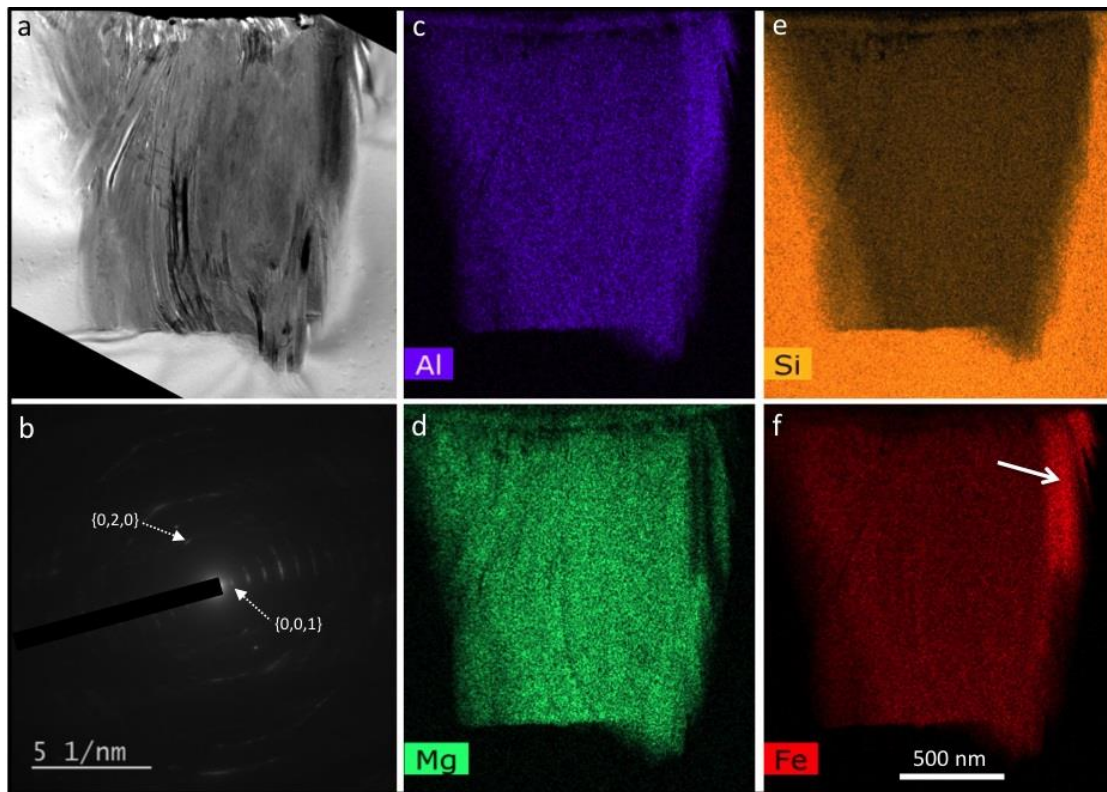
Figure 8. TEM analysis of a separate AIT, with the cross section extracted perpendicular to the direction of pyrite propulsion. a) Bright-field TEM image showing a typical polygonal cross sectional morphology. The infill of the microtube comprises multiple flaky grains of greater mass than the surrounding quartz matrix. b) Selected area electron diffraction pattern from the centre of the AIT encompassing several flaky grains; arcs towards the centre of the pattern come from a set of closely aligned crystals viewed along the <100> zone axis, and give d-spacings of 1.42 nm and 0.46 nm, representing the {001} and {020} crystallographic planes of monoclinic chlorite. c-f) ChemiSTEM elemental maps showing that the chlorite is dominantly Mg-rich (towards the clinochlore end member), but Fe-rich (towards the chamosite end member) in the top right portion of the AIT.
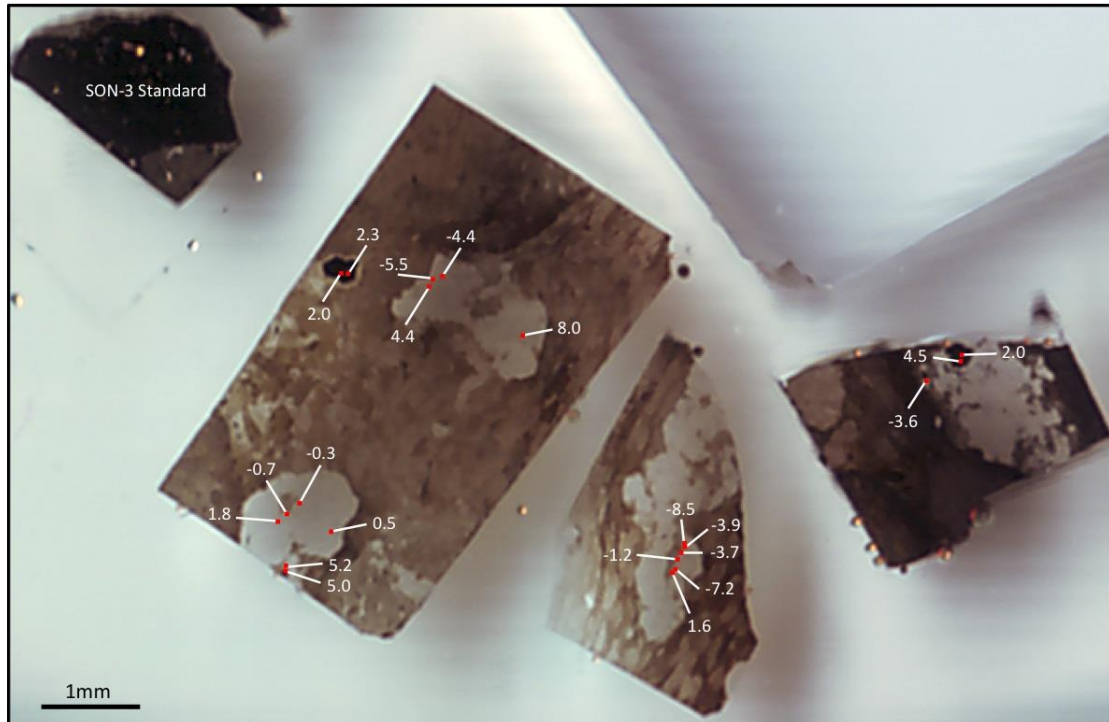
Figure 9. Overview of the mount used for NanoSIMS sulfur isotope analyses, showing locations and isotopic values, given as $\delta^{34}S_{\text{V-CDT}}$ (‰), of analysis areas N1-N21, plus the pyrite standard. Note, analyses N1-N6 are from larger pyrites adjacent to AIT, and N7-N21 are from pyrite grains actually within AIT. See Table 1 for complete sulfur isotope data set.

Table 1. NanoSIMS sulfur isotope results

Analysis ID	^{34}S counts	$\delta^{34}S_{V\text{-}CDT}$	±1σ (‰)
Standard	x10^6		
S1_1	5.03	2.2	0.9
S1_2	5.02	0.3	0.9
S1_3	4.99	0.1	0.9
S1_4	4.97	0.6	0.9
S1_5	5.21	1.8	0.8
S1_6	5.14	4.3	0.8
S1_7	5.14	0.6	0.8
S1_8	5.13	2.4	0.8
S1_9	5.19	0.7	1.0
S1_10	5.16	1.9	1.0
S1_11	5.66	3.0	0.6
S1_12	5.27	2.5	0.6
S1_13	5.20	0.1	0.6
S1_14	5.20	-0.4	0.7
S1_15	5.59	3.9	0.9
S1_16	5.27	2.2	1.0
S1_17	5.23	1.8	1.1
S1_18	5.19	0.3	1.2
S1_19	5.17	1.7	1.3
		Mean = 1.6	
		sd = 1.3	
Sample CBL10			
CBL_N1	3.71	2.3	0.9
CBL_N2	3.70	2.0	0.9
CBL_N3	3.85	5.2	0.8
CBL_N4	3.03	5.0	1.0
CBL_N5	3.55	4.5	0.9
CBL_N6	3.55	2.0	0.9
CBL_N7	3.58	-4.4	0.9
CBL_N8	3.68	-5.5	0.9
CBL_N9	5.00	4.4	0.8
CBL_N10	4.69	8.0	0.8
CBL_N11	6.48	1.8	0.8
CBL_N12	3.85	-0.7	1.0
CBL_N13	3.67	-0.3	1.0
CBL_N14	3.61	0.5	1.0
CBL_N15	1.54	-1.2	1.5
CBL_N16	1.48	-3.7	1.5
CBL_N17	3.64	-3.6	1.1
CBL_N18	5.75	-7.2	0.6
CBL_N19	5.52	1.6	0.7
CBL_N20	5.48	-8.5	0.8
CBL_N21	5.96	-3.9	0.8
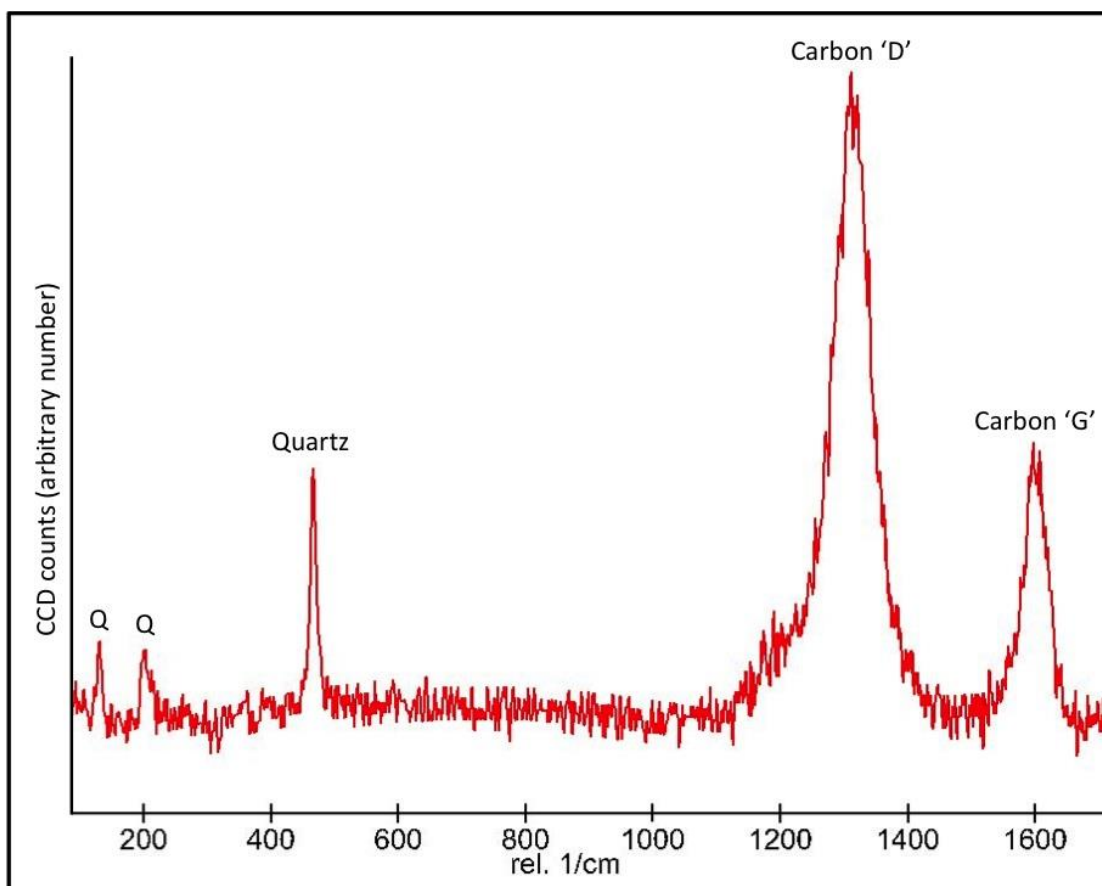
Supplementary Figure 1. Typical Raman spectrum of kerogen from the edge of a Current River AIT.
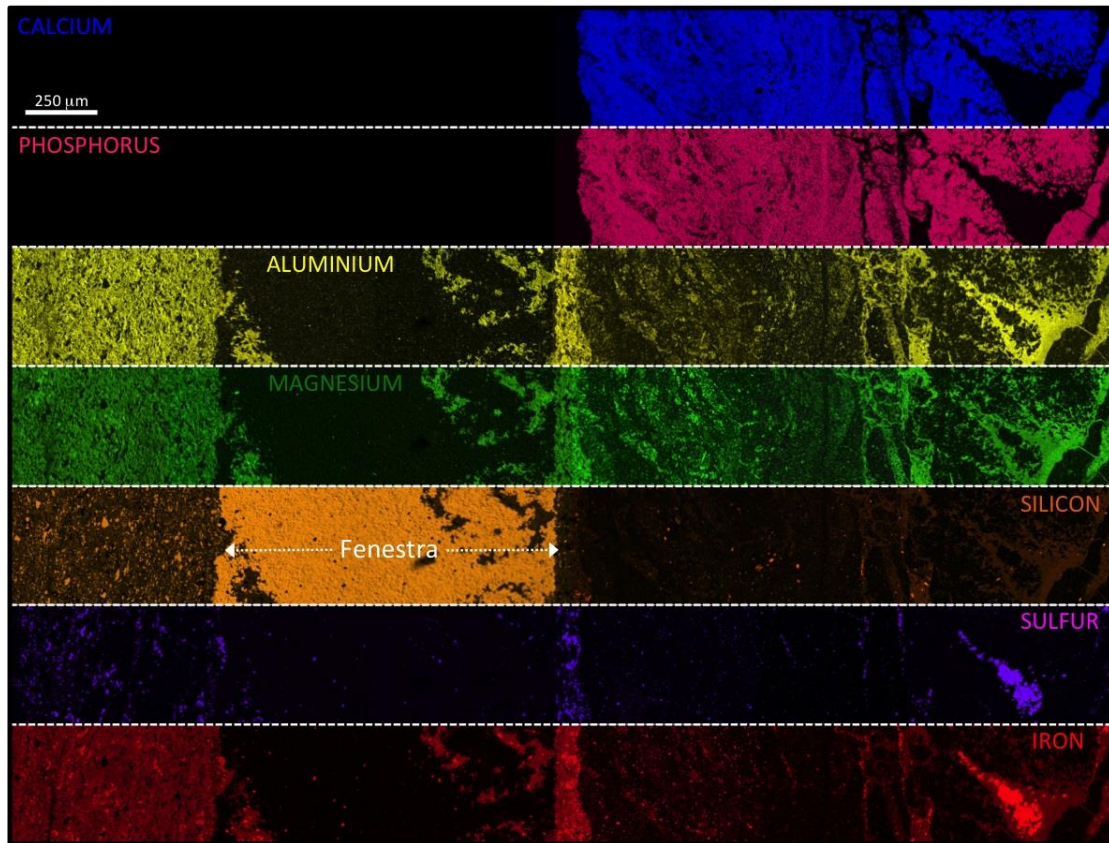
Supplementary Figure 2. Full set of EDS element maps from the area indicated by the green box in Figure 2d. Sulfur and the brightest iron areas correlate with one another and are indicative of pyrite. Aluminium and magnesium correlate with one another, and with moderate amounts of silicon and iron, indicative of chlorite. Calcium and phosphorus correlate with one another and are indicative of calcium phosphate (apatite). The fenestra is labeled and has the highest amount of silicon, indicative of a quartz mineralogy.